



AFRL-RZ-WP-TP-2012-0159

**THE INFLUENCE OF STOICHIOMETRY AND FLAME-HOLDER
SHAPE ON FLAME DYNAMICS AND ACOUSTICS (PREPRINT)**

Barry V. Kiel (AFRL/RZTP)

Amy Lynch (AFRL/RZTC)

Propulsion Branch (AFRL/RZTP)

Combustion Branch (AFRL/RZTC)

Turbine Engine Division

Stanislav Kostka

Spectral Energies, LLC

Beth Huelskamp

Innovative Scientific Solutions, Inc.

Reza Kashani and Nick Parr

University of Dayton

APRIL 2012

Approved for public release; distribution unlimited.

See additional restrictions described on inside pages

STINFO COPY

**AIR FORCE RESEARCH LABORATORY
PROPULSION DIRECTORATE
WRIGHT-PATTERSON AIR FORCE BASE, OH 45433-7251
AIR FORCE MATERIEL COMMAND
UNITED STATES AIR FORCE**

REPORT DOCUMENTATION PAGE

Form Approved
OMB No. 0704-0188

The public reporting burden for this collection of information is estimated to average 1 hour per response, including the time for reviewing instructions, searching existing data sources, gathering and maintaining the data needed, and completing and reviewing the collection of information. Send comments regarding this burden estimate or any other aspect of this collection of information, including suggestions for reducing this burden, to Department of Defense, Washington Headquarters Services, Directorate for Information Operations and Reports (0704-0188), 1215 Jefferson Davis Highway, Suite 1204, Arlington, VA 22202-4302. Respondents should be aware that notwithstanding any other provision of law, no person shall be subject to any penalty for failing to comply with a collection of information if it does not display a currently valid OMB control number. **PLEASE DO NOT RETURN YOUR FORM TO THE ABOVE ADDRESS.**

1. REPORT DATE (DD-MM-YY) April 2012	2. REPORT TYPE Technical Paper Preprint	3. DATES COVERED (From - To) 01 April 2010 – 01 April 2012
--	---	--

4. TITLE AND SUBTITLE THE INFLUENCE OF STOICHIOMETRY AND FLAME-HOLDER SHAPE ON FLAME DYNAMICS AND ACOUSTICS (PREPRINT)	5a. CONTRACT NUMBER In-house
	5b. GRANT NUMBER
	5c. PROGRAM ELEMENT NUMBER 62203F

6. AUTHOR(S) Barry V. Kiel (AFRL/RZTP) Amy Lynch (AFRL/RZTC) Stanislav Kostka (Spectral Energies, LLC) Beth Huelskamp (Innovative Scientific Solutions, Inc.) Reza Kashani and Nick Parr (University of Dayton)	5d. PROJECT NUMBER 3066
	5e. TASK NUMBER 05
	5f. WORK UNIT NUMBER 306605AR

7. PERFORMING ORGANIZATION NAME(S) AND ADDRESS(ES) Propulsion Branch (AFRL/RZTP) Combustion Branch (AFRL/RZTC) Turbine Engine Division Air Force Research Laboratory, Propulsion Directorate Wright-Patterson Air Force Base, OH 45433-7251 Air Force Materiel Command, United States Air Force	8. PERFORMING ORGANIZATION REPORT NUMBER AFRL-RZ-WP-TP-2012-0159
--	--

9. SPONSORING/MONITORING AGENCY NAME(S) AND ADDRESS(ES) Air Force Research Laboratory Propulsion Directorate Wright-Patterson Air Force Base, OH 45433-7251 Air Force Materiel Command United States Air Force	10. SPONSORING/MONITORING AGENCY ACRONYM(S) AFRL/RZTP
	11. SPONSORING/MONITORING AGENCY REPORT NUMBER(S) AFRL-RZ-WP-TP-2012-0159

12. DISTRIBUTION/AVAILABILITY STATEMENT Approved for public release; distribution unlimited.
--

13. SUPPLEMENTARY NOTES Paper contains color. PA Case Number: 88ABW-2010-6517; Clearance Date: 14 Dec 2010.
--

14. ABSTRACT Combustion instability manifests itself by the coupling of heat release and chamber acoustics. These instabilities can be present in any type of combustion system, including gas turbine engines, scramjet engines, and industrial furnaces and boilers. Much research has been conducted on the coupling of acoustics and heat release for lean-burning systems. Historically, models of these systems assume the flames to be short and the mean fields to be incompressible. Proposed here is a new approach to coupling dynamics. If the governing equations are considered to be compressible, then a relationship among acoustics, vorticity, and pressure can be derived. In this study the relationship among vortex shedding, flame dynamics, and acoustics is explored for a bluff-body-stabilized flame using high-speed flame images and high-speed pressure transducers. It is demonstrated that the flame radiates sound over a broad spectrum and that thermoacoustic coupling occurs when the flame sound radiation couples with one of the modes of the combustion chamber.
--

15. SUBJECT TERMS augmentor, dynamic stability, screech, flame holder, gas-turbine propulsion, combustion

16. SECURITY CLASSIFICATION OF:			17. LIMITATION OF ABSTRACT: SAR	18. NUMBER OF PAGES 24	19a. NAME OF RESPONSIBLE PERSON (Monitor) Barry V. Kiel
a. REPORT Unclassified	b. ABSTRACT Unclassified	c. THIS PAGE Unclassified			

The Influence of Stoichiometry and Flame-Holder Shape on Flame Dynamics and Acoustics

Barry Kiel¹ and Amy Lynch²
*Air Force Research Laboratory
Wright-Patterson Air Force Base, OH 45433*

Stanislav Kostka³
*Spectral Energies, LLC.
Dayton, OH 45431*

Bethany Huelskamp⁴
*Innovative Scientific Solutions, Inc.
Dayton, OH 45440*

Reza Kashani⁵ and Nick Parr⁶
*University of Dayton
Dayton, OH 45469*

Combustion instability manifests itself by the coupling of heat release and chamber acoustics. These instabilities can be present in any type of combustion system, including gas turbine engines, scramjet engines, and industrial furnaces and boilers. Much research has been conducted on the coupling of acoustics and heat release for lean-burning systems. Historically, models of these systems assume the flames to be short and the mean fields to be incompressible. Proposed here is a new approach to coupling dynamics. If the governing equations are considered to be compressible, then a relationship among acoustics, vorticity, and pressure can be derived. In this study the relationship among vortex shedding, flame dynamics, and acoustics is explored for a bluff-body-stabilized flame using high-speed flame images and high-speed pressure transducers. It is demonstrated that the flame radiates sound over a broad spectrum and that thermoacoustic coupling occurs when the flame sound radiation couples with one of the modes of the combustion chamber.

I. Introduction

Combustion instability manifests itself in many of today's combustors. Instabilities have been reported in all types of propulsion systems, including rockets, scramjets, gas turbine combustors, and augmentors. Throughout the 50-year development of high-performance gas turbine engines, combustion instability has been a major challenge with regard to both the combustor and the thrust augmentor. Over the same time period, many advances have been made in the modeling of combustion instability.

¹Traditional thermoacoustics modeling is based on Culick's framework (Candel 2002, Malhotra 2004) where both the pressure fluctuations and the Mach number of the flow in the combustion chamber are assumed to be small. These assumptions result in a wave equation that describes wave propagation in the combustion chamber, forced by an unsteady heat-release term. This type of model has proven to be very effective in systems where the Mach number is small.

In this investigation time-evolving flame and acoustic pressure were studied. Simultaneous flame images from a Phantom 7.1 camera and acoustic pressure signals from high-speed Kulite transducers were obtained over a

¹ Corresponding Author, Senior Engineer, Senior AIAA member

² Combustion Research Engineer, AIAA member

³ Research Engineer, AIAA member

⁴ Research Engineer, AIAA member

⁵ Professor, Senior AIAA member

⁶ Graduate Student, AIAA member

wide range of conditions and with several different flame-holder shapes. Spectral analysis was used to study the cause-and-effect relationship between the various flame-vortex modes and the acoustics. Three separate flame/acoustic/vortex phenomena were studied: the influence of stoichiometry, inlet temperature, and boundary-layer development. Vortex shedding and flame coupling were found to vary widely as these three parameters were varied.

II. Compressibility, Vorticity, Noise, and Heat Release

Examination of the governing equations for mass momentum, energy, and vorticity sheds some light on the coupled nature of vorticity and the flame. The diffusion flames discussed in the introduction operated at very low velocity, on the order of 10 s of meters a second. As a result these studies assumed an incompressible formulation. Equation (1) is the conservation equation for mass. For incompressible flow the density is constant and, thus, the divergence of velocity; the right-hand side of Eq. (1) is zero. For compressible flow the divergence of the velocity is nonzero and related to the compressibility of the flow.

$$\frac{\partial \rho}{\partial t} + \nabla \cdot \rho V = -\rho \nabla \cdot V \quad (1)$$

Upon studying the vorticity equation, one observes a source term that relates vorticity generation to velocity divergence. Net compression of the fluid element results in an amplification of the vorticity. Equation (1) can be manipulated further to show a relationship among vorticity, unsteady pressure, and heat release. If Eq. (1) is written in terms of the acoustic density and velocity (Kiel 2008):

$$\frac{\partial \dot{\rho}}{\partial t} + \bar{V} \nabla \cdot \dot{\rho} = -\bar{\rho} \nabla \cdot \bar{V} - \bar{\rho} \nabla \cdot \dot{V} - \dot{\rho} \nabla \cdot \bar{V} \quad (2)$$

Acoustic pressure and density are related through the definition for wave speed, Eq. (3). Note that the density fluctuations are small and assumed to be two to three order of magnitude smaller than the mean density.

$$d\dot{\rho} = a^2 d\dot{p} \quad (3)$$

Using Eq. (3) and the assumption, Eq. (2) is converted to an equation for acoustic pressure. The resultant equation is:

$$\frac{\partial \dot{p}}{\partial t} + \bar{V} \nabla \cdot \dot{p} = -a^2 \bar{\rho} \nabla \cdot \bar{V} - a^2 \bar{\rho} \nabla \cdot \dot{V} \quad (4)$$

Equation (4) contains two sources of pressure fluctuations from velocity divergence: one source of pressure fluctuations from the divergence of the mean flow velocity and another from the divergence of acoustic velocity. Note that small amounts of divergence can result in large acoustic pressure fluctuations because the divergence term is multiplied by the square of the wave speed. In terms of divergence of the mean velocity Eq. (4) becomes:

$$\frac{\frac{\partial \dot{p}}{\partial t} + \bar{V} \nabla \cdot \dot{p} + a^2 \bar{\rho} \nabla \cdot \dot{V}}{a^2 \bar{\rho}} = -\nabla \cdot \bar{V} \quad (5)$$

Substituting Eq. (5) into the vorticity equation results in:

$$\begin{aligned} \frac{\partial \omega}{\partial t} + (V \cdot \nabla) \omega = & \\ & (\omega \cdot \nabla) V - \\ \omega \left(\frac{\frac{\partial \dot{p}}{\partial t} + \bar{V} \nabla \cdot \dot{p} + \gamma \bar{p} \nabla \cdot \dot{V}}{\gamma \bar{p}} \right) & \\ \frac{1}{\rho^2} \nabla \rho \times \nabla p + \nabla \times (\nabla \cdot \tau) & \end{aligned} \quad (6)$$

In the absence of combustion, spatial and temporal acoustic pressure fluctuations clearly cause vorticity fluctuations and vice versa. The equations for conservation of mass, momentum, and energy with heat release are:

$$\frac{\partial \rho}{\partial t} + \nabla \cdot (\rho V) = 0 \quad (7)$$

$$\frac{\partial(\rho V)}{\partial t} + \nabla \cdot (\rho V V) = -\nabla p + \mu \nabla \cdot \nabla V \quad (8)$$

$$\rho \frac{\partial e}{\partial t} + \rho V \nabla \cdot e = -p \nabla \cdot V + q \quad (9)$$

In Eq. (9), “q” is the heat release from combustion. An equation for pressure, Eq. (10), can be derived using Eqs. (7) and (9).

$$\frac{\partial p}{\partial t} + V \nabla \cdot p = -\gamma p \nabla \cdot V + (\gamma - 1)q \quad (10)$$

Solving for the velocity divergence:

$$\frac{((\gamma-1)q - \frac{\partial p}{\partial t} - V \nabla \cdot p)}{\gamma p} = \nabla \cdot V \quad (11)$$

Substituting Eq. (11) into the vorticity equation results in:

$$\begin{aligned} \frac{\partial \omega}{\partial t} + (V \cdot \nabla) \omega = & \\ & (\omega \cdot \nabla) V \\ - \omega \left(\frac{((\gamma-1)q - \frac{\partial p}{\partial t} - V \nabla \cdot p)}{\gamma p} \right) & \\ + \frac{1}{\rho^2} \nabla \rho \times \nabla p + \nabla \times (\nabla \cdot \tau) & \end{aligned} \quad (12)$$

In this equation, unsteady vorticity, unsteady pressure and heat release are all related. This further demonstrates that vorticity is a significant source of unsteady heat release. This analysis of the governing equations reinforces the conclusions in that vorticity fluctuations are a driver for the stability and instability of bluff body flames. Clearly ignoring compressibility, like most researchers do, has caused this coupling mechanism to be largely overlooked in the literature.

III. Experimental Setup

A 4-MW experimental atmospheric combustion facility located in the Propulsion Directorate of the Air Force Research Laboratory (AFRL) at Wright-Patterson AFB was used for the experiments. The facility enables the simulation of geometries ranging from simple, two-dimensional, research flame-holder concepts to complicated, engine-like three-flame-holder sectors. Electrical heaters can supply air-inlet temperatures up to 800 R, and the facility has a vitiator that can supply vitiated air up to 1800 R. Oxygen concentration can be varied from 15 to 21 percent. Available air flow allows combustion research at Mach numbers up to 0.4, Reynolds numbers up to 100,000, and modified DeZubay correlation parameters, Eq. (13), up to 100. Figure 1 is a photo of the rig installed in the Atmospheric Pressure Combustion research Facility.

$$Dz = \frac{10,000U}{p^{0.95} T^{1.2} L^{0.85}} \quad (13)$$

Many fuels are available for research. Gaseous propane and methane can be premixed upstream of the flame holders. Three liquid-fuel pumps are available to flow a host of liquid fuels, including JET A/JP-8 as well as synthetic and bio-derived jet fuels.

Figure 2 is a schematic of the experimental rig with the v-gutter bluff-body flame holder installed. The air flow in the rig is from right to left in the photograph. The rig is 41 in. long and the cross section is 6 in. high by 5 in. wide. A perforated plate is installed 3 in. downstream from the inlet to provide flow straightening and setting of turbulence levels. Fuel injection is located 20 perforation diameters downstream of the perforated plate. The liquid fuels atomize and as they convect downstream and droplets are vaporized prior to combustion behind the flame holder. The flame holders are mounted to the side walls of the rig, and their trailing edge is 23 in. from the inlet to the rig.

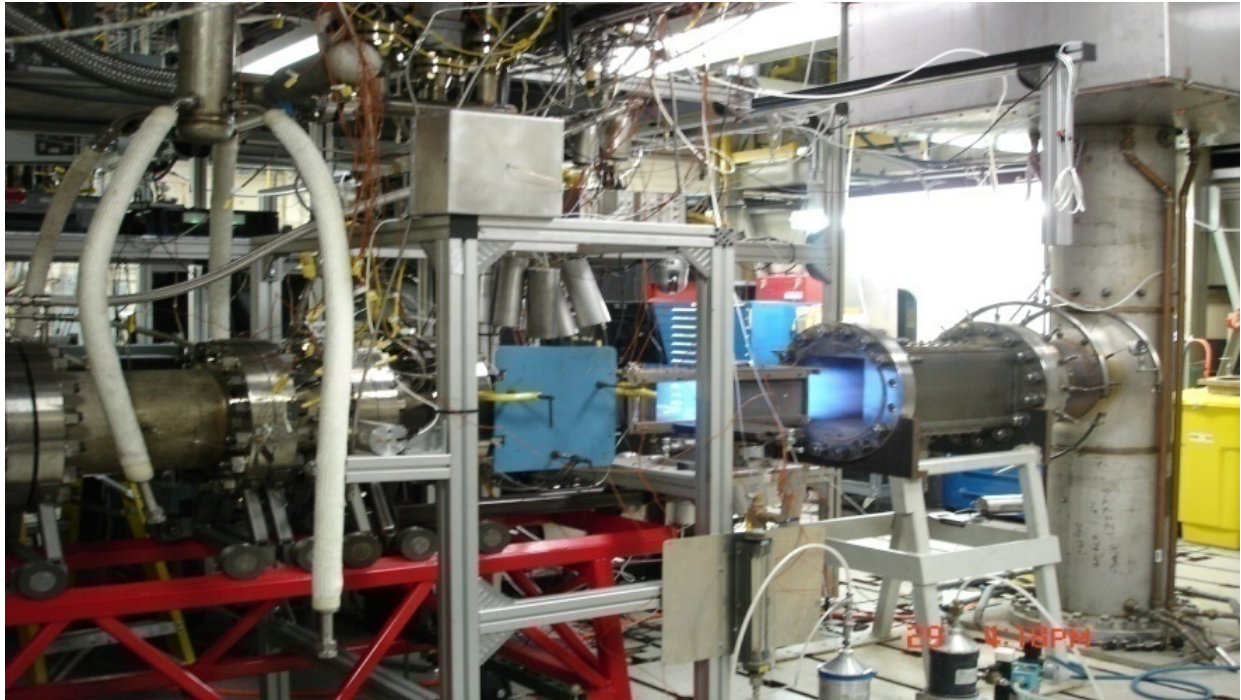


Figure 1. Bluff-body flame rig installed in atmospheric-pressure research facility.

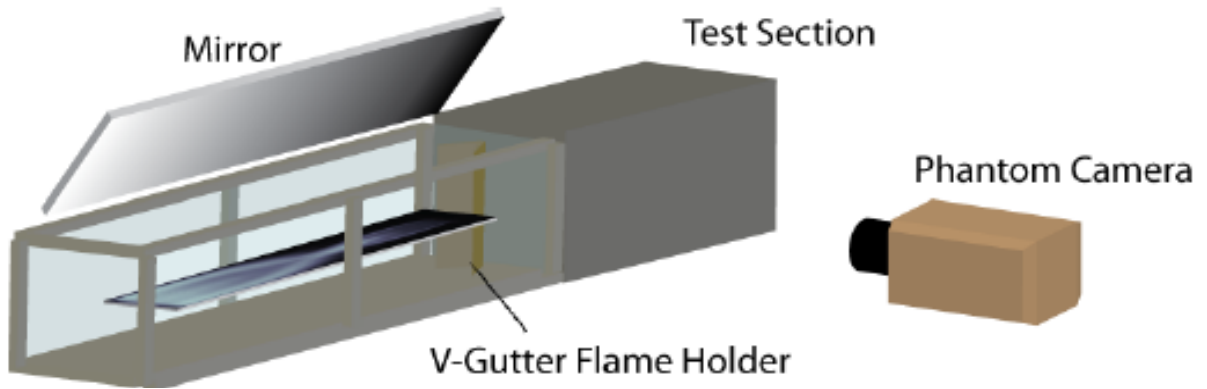


Figure 2. Schematic of bluff-body rig, showing optical access and high-speed-camera placement.

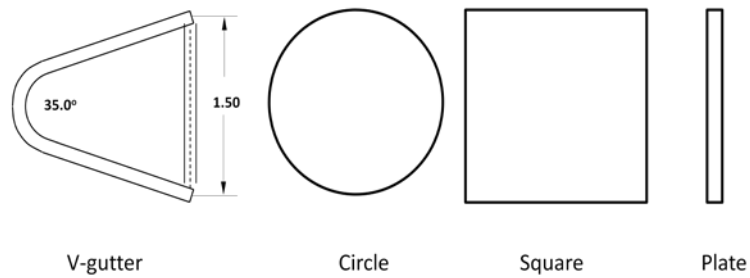


Figure 3. Bluff-body flame holders.

In this research the influence of vortex-shedding modes was studied. To investigate the impact of boundary-layer/shear-layer development on the flame, different flame-holder geometries with different boundary-layer/shear-layer development were tested. Figure 3 depicts flameholder geometries with different boundary layers. The v-gutter has a boundary layer that develops from the small-radius leading edge. The thickness of the boundary layer is a function of the Reynolds number of the oncoming air. For the square flame holder, the boundary-layer thickness is also a function of the Reynolds number, but its initiation and development are the result of the trip from the corner of the leading face. In both cases the position of the boundary layer on the downstream side of the flame holder is constant. For the circular cylinder, the thickness of the boundary layer is also a function of the Reynolds number, as in the case of the v-gutter and the square. The location where the boundary layer separates on the downstream side of the flame holder, however, is not constant and is a function of the Reynolds number. The scale of the v-gutter and square flame holders can also be changed to study the effects of the development length on the stability. Finally, the plate, similar to the turbulent diffusion flames in the literature (Chaudhuri and Cetegen, 2009 and Chaparro et al., 2006), has little or no boundary layer. This allows the study of flame stabilization in the absence of the boundary layer as a control.

IV. High-Speed Imaging and Pressure Procedures

For the study of thermoacoustic instabilities, high-speed pressure measurements are employed in conjunction with high-speed diagnostics to ascertain the coupling between the acoustic modes, heat-release hydrodynamics, and vorticity. High-speed images are synchronized with high-speed pressure transducers through the efficient use of LabVIEW hardware and software, with simultaneous software triggering.

High-speed images are acquired using of high-speed video and a Phantom v7.1 high-speed camera from Vision Research. The camera can be used to capture high-speed visible or filtered light images. The camera is a 12-bit SR-CMOS monochrome camera with a Gigabit Ethernet connection that is capable of capturing video at a maximum resolution of 800 x 600 pixels at 4800 frames per second (fps). For smaller images, repetition rates up to 160,000 fps can be achieved.

Acoustic pressure measurements can be made using fast Kulite pressure transducers up to 40 kHz. Because of the hot surfaces on the rig, high-speed pressure transducers cannot be flush mounted to the experimental rig. As a result, Semi-Infinite Transducers (SITs) with a standoff capability are employed (Fig. 4). In each of the SITs, a Kulite 5-psi differential pressure transducer that is capable of measuring acoustic pressure fluctuations up to 40 kHz is mounted in a stainless-steel "tee". On the left side of the tee is a 0.3-m standoff that connects to the rig. The right side of the tee connects to the differential side of the transducer. This connection is made with a coiled small-diameter tube that is 10 m long. The length of the coiled tube provides sufficient acoustic compliance that the pressure on the differential side of the transducer is constant.

Fifteen SITs are mounted longitudinally along the rig. Simultaneous high-speed measurements of multiple SITs are made with a high-speed data-acquisition system. An M-series NI 6280 Multi-function Data Acquisition (DAQ) board is installed into a computer. This board has 16 analog input channels, with a maximum sampling rate of 625 kHz and 18-bit resolution. To enable multi-channel simultaneous sampling, the 6280 board is linked to an SCXI 1000 chassis, which is configured with two 8-channel SCXI 1140 boards. The 1140 boards are capable of simultaneous sampling of all eight input channels with less than 3-ns delay between channels. The SCXI chassis also houses four SCXI 1121 Isolated Universal Input Modules. Each SCXI 1121 board has four input channels. The leads from the Kulite pressure transducers in each of the SITs are attached to a terminal block that is mounted to the front of each 1121 board. The 1121 boards supply 10-V excitation to power the transducers. Two of the 1121 boards are connected to an 1140 board on the back plane of the SCXI. The DAQ is capable of reading all of the 1140s simultaneously. As a result the system allows the simultaneous read of up to 16 Kulite transducers. Simultaneous high-speed triggering of the SITs and Phantom 7.1 camera is accomplished through an external hardware TTL pulse.



Figure 4. Schematic and photograph of Semi-Infinite Transducers (SITs).

V. Acoustic Model Utilizing Comsol

The wave-propagation equations were derived from the Euler equations. Using the perturbation relationship for any variable “a”, the mean and acoustic

$$a = \bar{a} + a' \quad (14)$$

component can be derived. To obtain the final perturbation equations, it was assumed that the second-order fluctuating quantities were zero, the density was constant, there was only axial mean velocity, and the viscous forces due to acoustic velocity were small. The resulting acoustic pressure and velocity equations are:

$$\frac{1}{a^2} \frac{\partial p'}{\partial t} + \bar{\rho} \frac{\partial u'}{\partial x} + \frac{\bar{u}}{a^2} \frac{\partial p'}{\partial x} + \bar{\rho} \frac{\partial v'}{\partial y} + \bar{\rho} \frac{\partial w'}{\partial z} = 0 \quad (15)$$

$$\bar{\rho} \frac{\partial u'}{\partial t} + \bar{\rho} \bar{u} \frac{\partial u'}{\partial x} + \bar{\rho} v' \frac{\partial \bar{u}}{\partial y} + \bar{\rho} w' \frac{\partial \bar{u}}{\partial z} = -\frac{\partial p'}{\partial x} \quad (16)$$

$$\bar{\rho} \frac{\partial v'}{\partial t} + \bar{\rho} \bar{u} \frac{\partial v'}{\partial x} = -\frac{\partial p'}{\partial y} \quad (17)$$

$$\bar{\rho} \frac{\partial w'}{\partial t} + \bar{\rho} \bar{u} \frac{\partial w'}{\partial x} = -\frac{\partial p'}{\partial z} \quad (18)$$

The equation for wave propagation with mean flow and shear results from taking the time derivative of Eq. (15) and the derivative with respect to x,y,z of Eqs. (16), (17), and (18), respectively. The resulting wave equation is:

$$\begin{aligned}
& \frac{\partial^2 p'}{\partial t^2} + 2Ma \frac{\partial^2 p'}{\partial x \partial t} - a^2 [1 - M^2] \frac{\partial^2 p'}{\partial x^2} \\
& - a^2 \frac{\partial^2 p'}{\partial y^2} - a^2 \frac{\partial^2 p'}{\partial z^2} \\
& - 2\bar{\rho}a^3 \frac{\partial v'}{\partial x} \frac{\partial M}{\partial y} - 2\bar{\rho}a^3 \frac{\partial w'}{\partial x} \frac{\partial M}{\partial z} = 0
\end{aligned} \tag{19}$$

The three-dimensional wave equation without flow is represented by the first, third, fourth, and fifth terms on the left-hand side of Eq. (19). The remaining terms on the left-hand side of Eq. (19), which have Mach numbers in them, represent the damping due to mean flow. The terms with the transverse derivative of the mean axial velocity are negative and represent damping due to these gradients (Kiel and Kashani, 2008). Clearly, Mach number and compressibility are key, even at low Mach numbers.

The mean axial velocity and temperature field of the experimental rig can be obtained using computational methods. A Fluent case was set for the experimental rig with a 1.5-in. v-gutter near the center. The RANS solver in Fluent was iterated to a converged solution. The k-epsilon turbulence model was used for closure. The Eddy Breakup Model was used for combustion closure. The Reynolds number for the simulation was $\sim 35,000$, and the equivalence ratio was ~ 0.6 . Figure 5 shows the mean temperature field from the Fluent solution; contours are in degrees Kelvin. Figure 6 is the mean axial velocity from the same Fluent solution; contours are in meters per second.

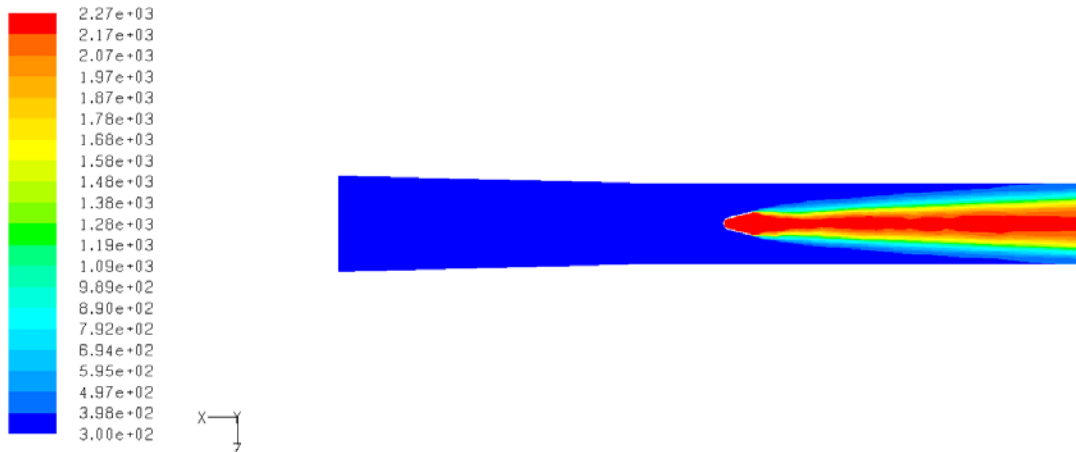


Figure 5. Contours of mean temperature in experimental rig from Fluent.

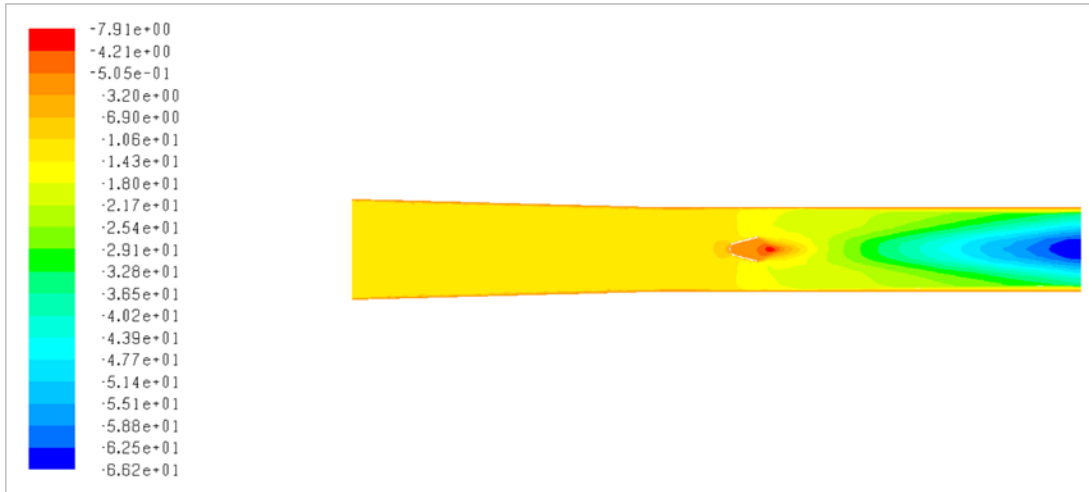


Figure 6. Contours of mean axial velocity in experimental rig from Fluent.

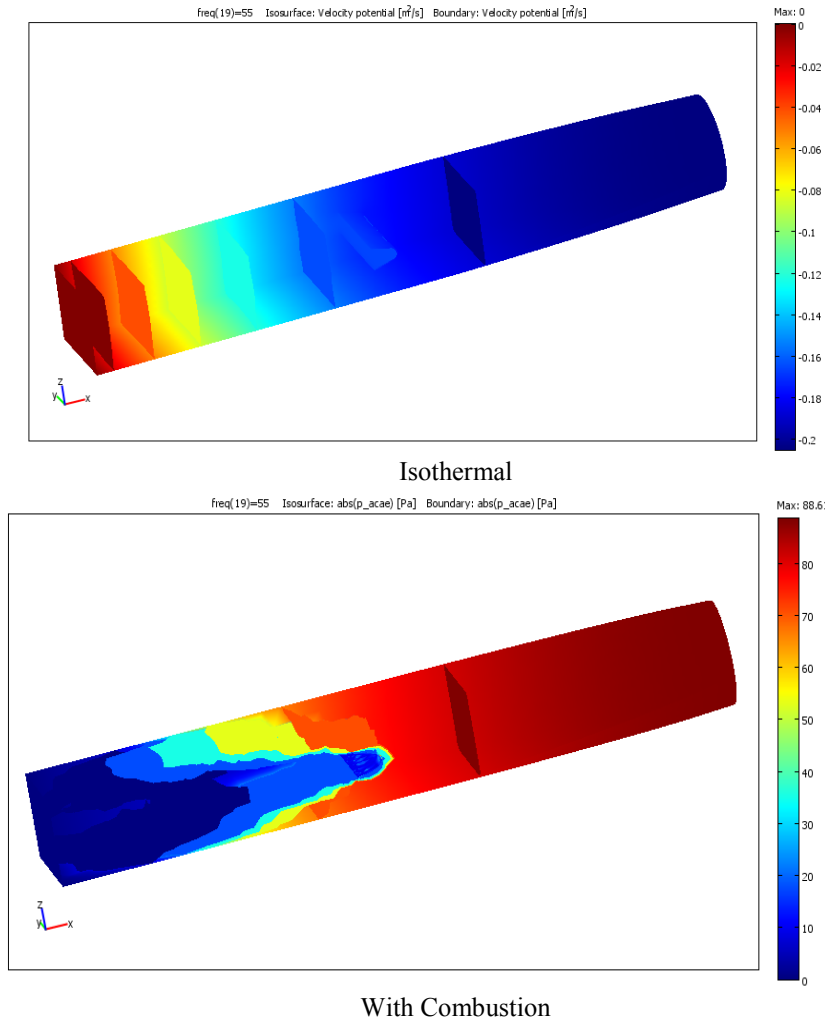
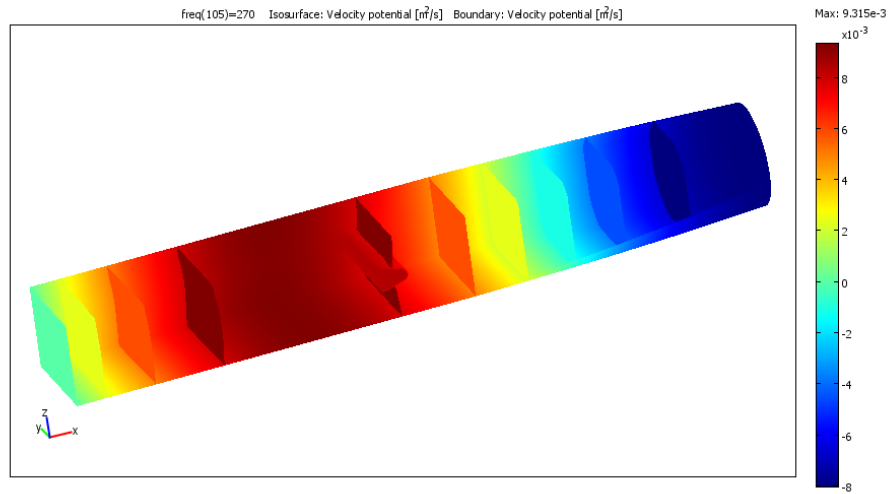
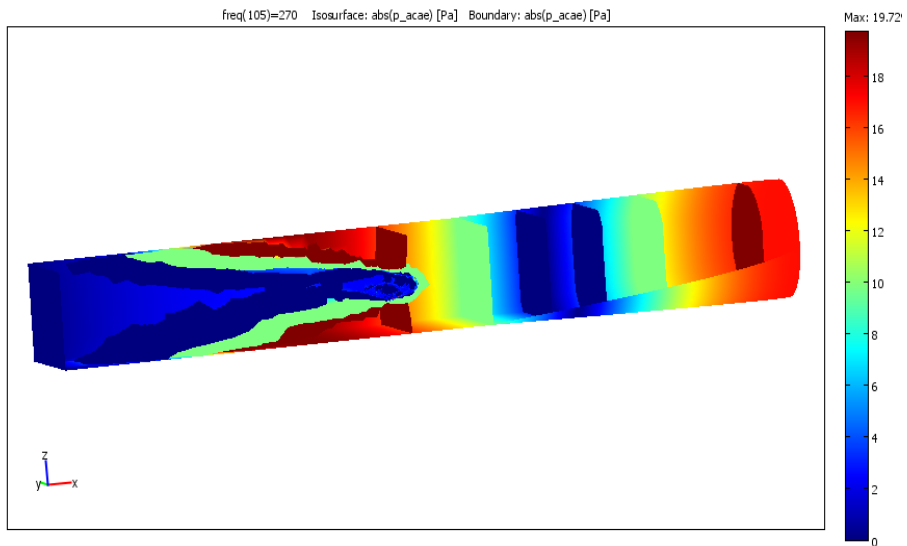


Figure 7. First axial mode of experimental rig.



a) Isothermal



With Combustion

Figure 8. Second axial mode of experimental rig with mean flow and combustion.

The finite-element software package COMSOL Multiphysics was used to find the acoustic modes of the experimental rig. The PDE mode of COMSOL was used to solve Eqs. (15 - (18). The mean temperature and axial velocity from the Fluent solutions in Figs. 5 and 6 were imported into COMSOL. A mesh of the experimental rig was generated in COMSOL. Figures 7 and 8 are the shapes of the first two modes of the experimental rig. The top figure is the COMSOL isothermal solution with no mean flow. The second image in each is the COMSOL solution for the combusting rig using the velocity and temperature results from Fluent.

Figure 9 illustrates the modeled frequency response of the rig from COMSOL and the cross spectrum of pressure from SITs mounted to the rig. The blue line in the left-hand plot of Fig. 9 corresponds to the frequency response of the isothermal case with no flow. The red line represents the combusting case with flow. Note that the addition of mean flow damps the peaks of the modes. It should also be noted that combustion shifts the resonant frequency of the modes because of an increase in the wave speed in the combustion zone. The frequency of the first mode is reduced, while the frequencies of the subsequent higher harmonics increase. The frequency of the first mode should have also increased. The decrease in frequency of the first mode must be explored further. The right-hand side of Fig. 9 illustrates the experimental data taken with the SITs for isothermal conditions at 300K. The figure depicts the auto spectrum of the first transducer nearest the pressure antinode. Note the good agreement between the frequencies from the rig spectral data and those from the isothermal results (blue trace) from the

COMSOL model data. Small adjustments to the COMSOL solution are required to obtain a better match with the actual damping and, thus, bandwidth of the experimental data. Clearly the modes are closed open in Figs. 7 and 8. This is verified by the odd-integer separation of the peaks in the model and the experimental data depicted in Fig. 9.

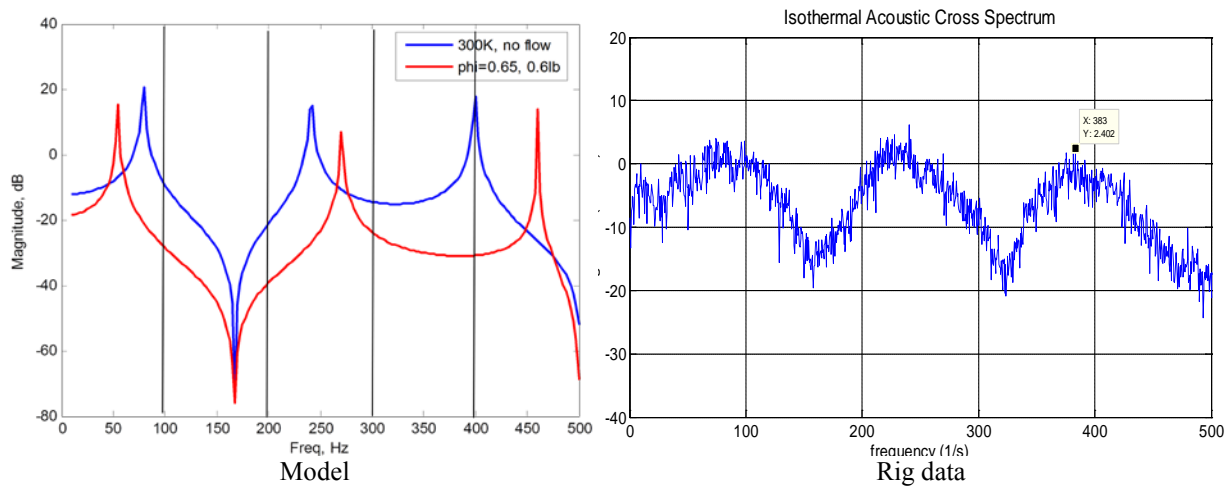


Figure 9. Frequency response (model) and cross spectrum (rig) of experimental rig.

VI. High-Speed Images

Figures 10, 11, and 12 are high-speed images of the flame luminosity that were obtained with the high-speed Phantom 7.1 camera. These were taken under room-temperature inlet conditions corresponding to a Reynolds number of $\sim 35,000$. In each figure the 1.5-in. v-gutter flame holder was used to stabilize the flame. In Fig. 10 the equivalence ratio is ~ 0.8 , and the flame is very near the lean limit. Figure 11 contains images from the same experiment, with an equivalence ratio of ~ 0.6 . Figure 23 contains a series of images for the same experimental conditions, except that the equivalence ratio is ~ 1.0 .

Evaluating to Eq. (12) several sources of and sinks of vorticity exist. When a flame is present, the heat release is a source term. The cross product of pressure and density is also a source of vorticity; thus, density gradients properly aligned cause vortex generation. Upstream of the flame, Kelvin-Helmholtz vortices are generated by viscous shear and divergence of velocity at the wall of the bluff body. In Fig. 10, it appears that as the vortex leaves the trailing edge of the flame holder, the flame becomes anchored in the Kelvin-Helmholtz vortices leaving the lip of the flame holder are the size of the developed boundary layer and are small. As they convect through the flame, they appear to be amplified. The image is of the luminescent spectrum of the flame, not the velocity or vorticity.

Unlike isothermal flow, the flame creates a density gradient normal to the flame surface. The decrease in density across the flame results in an acceleration of the flow across the flame, increasing the flow velocity. The result is a large gradient and divergence of velocity across the flame. The density gradient across the flame is also a source of vorticity in the near field of the flame holder. In this region the density gradient and axial-pressure gradient are nearly perpendicular. The cross product of these two gradients results in a source of baroclinic vortices. The strength of the baroclinic term is dependent on the density or temperature ratio across the flame. Conspicuously missing from the image are the Von-Karman vortices generated in the isothermal wake. The magnitude of the changing sign of the divergence in the wake and the magnitude of the baroclinic generation are unknown. Thus, the reason for the suppression of the large Von-Karman vortices is unclear.

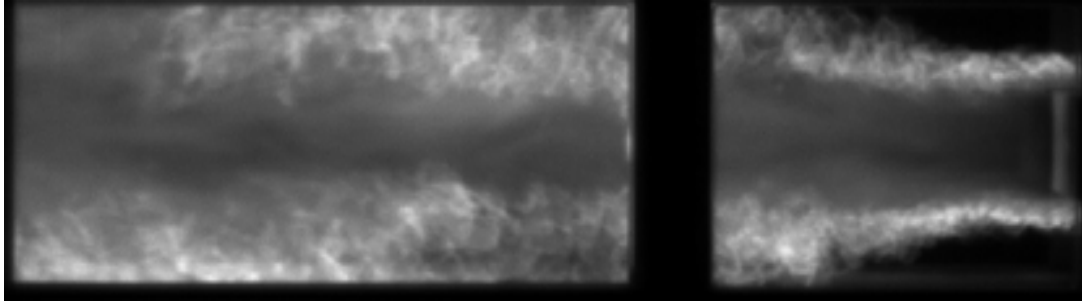


Figure 10. High-speed image of v-gutter-stabilized flame for equivalence ratio of ~0.8.

Figure 11 depicts the same conditions as those in Fig. 10, except that the equivalence ratio is very near blowout. As the equivalence ratio is decreased, larger vortices in the wake dominate the flame; these vortices are similar to Von-Karman vortices just before extinction. Further reductions in stoichiometry at this point result in flame extinction. Mehta and Soteriou (2003), Erickson, et al. (2006), and Sankaran et al. (2009) modeled vorticity behind bluff-body flames and have commented on vortex shedding. In their work, they concluded that the baroclinic vortices produced by a large temperature rise across the flame dominate and suppress the Von-Karman-type vortex shedding that is typically observed behind these bluff bodies under isothermal conditions. In their model they artificially change the density gradient across the flame. For density gradients < 2 , the wake becomes dominated by Von-Karman vortices. Shanbhogue et al. (2009) also comment that these vortices are possible mechanisms for the final extinction of the flame because of high strain.

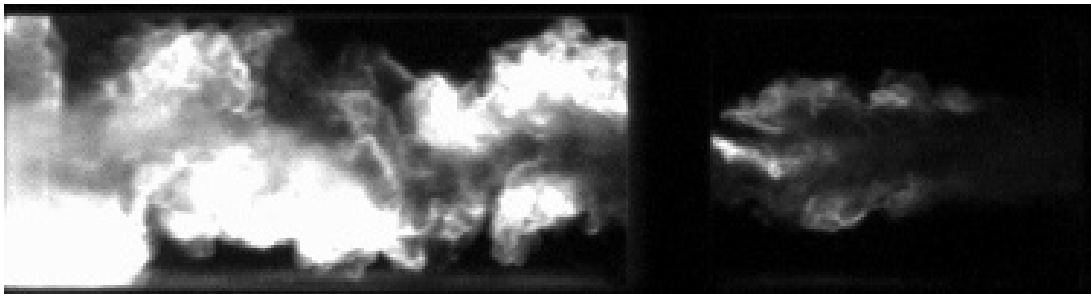


Figure 11. High-speed image of v-gutter-stabilized flame for equivalence ratio of ~0.6

Flames driven by thermoacoustic coupling have the same vorticity generation mechanisms as the flames discussed. These flames also have other vorticity-driving mechanisms due to oscillating acoustic pressure and velocity. The standing acoustic pressure and velocity waves establish gradients in pressure and velocity along the axis of the mode; the acoustic gradients are time varying. At any instant in time, the acoustic pressure and velocity decrease spatially from the antinode to the node. The acoustic pressure and velocity also oscillate everywhere in time. The greatest temporal oscillations in pressure occur at the antinode. Axially changing acoustic velocity can cause locally varying vorticity because of divergence of the acoustic velocity field--in much the same way as in the isothermal case. The locally varying vorticity due to acoustic velocity also changes in time because of the oscillating nature of the acoustic velocity.

Figure 12 shows four successive images of the luminosity of the flame for the same flame holder as in Figs. 10 and 11. In these images the flame is experiencing self-excited thermoacoustic oscillations. The images were taken 0.1 ms apart with a high-speed camera. For these images the Reynolds number is the same as in Figs. 10 and 11, and the equivalence ratio is 1.0. The frequency of the instability was measured to be 112 Hz. From acoustics, this frequency corresponds to the first longitudinal mode of the rig, assuming closed open boundaries. In the images in Fig. 12, the flame near the flame holder is dominated by two large vortices of opposite sign that are shed simultaneously from the flame holder. The shed vortices, as shown in the successive photos, grow and travel together downstream at the velocity of the mean flow. These vortices may have been generated from two possible sources in the shear layer of the flame holder (Kelvin-Helmholtz) or in the wake (Von Karman). The large convecting near-field vortices could also be baroclinic, induced by the cross product of the flame density gradient and the axial gradients in pressure (mean pressure gradient and acoustic pressure gradient).



Figure 12. Successive high-speed image of v-gutter-stabilized flame for equivalence ratio of ~ 1.0 .

VII. Spectrum Results

The high-speed SIT and camera luminosity images allow spectral and frequency-response analysis of the data. Figure 13 contains the cross-spectrum SIT data for the 3/2-in. v-gutter flame holder near blow out (left) and at an equivalence ratio of ~ 1.0 , where the first longitudinal mode is excited (right). For the flame near blow out, the sound spectrum has significant energy in the low-frequency spectrum below 300 Hz. Also note a peak in the spectrum near 150 Hz. According to Huelskamp et al. (2010), the Strouhal number for a v-gutter at the inlet Reynolds number for this experiment is ~ 0.25 , which corresponds to a shedding frequency of ~ 155 Hz. It appears from the data that there is sound radiation in the low frequency, with a peak at the Strouhal number of the flame holder.

The right-hand plot of Fig. 13 is for the same flame holder at the same conditions, except that the equivalence ratio is near 1.0 and the rig is thermoacoustically excited. Note that the spectrum above 0 dB now extends down to 500 Hz. Also note several peaks in the pressure data. The peak in the pressure spectrum is at the resonant frequency and probably represents the resonant mode. Clearly, however, other peaks exist in the pressure spectrum. It appears from the data that flame holder with the higher equivalence ratio radiated sound over a wider

spectrum and that several peaks are present in the pressure being radiated. The cause of these peaks is unclear. Heat-release and vorticity data are required before proper conclusions can be drawn as to their origin.

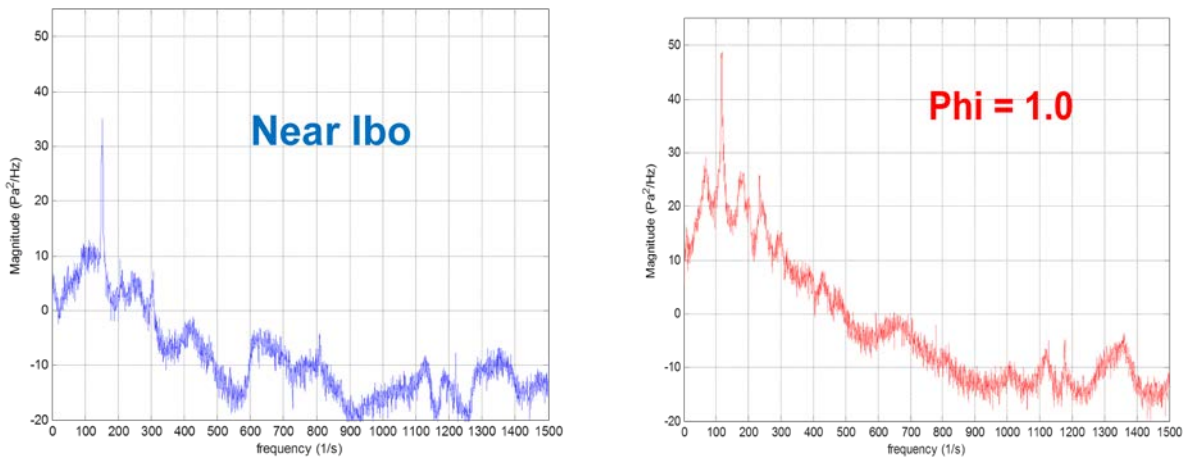


Figure 13. Magnitude of cross power spectrum of SIT acoustic pressure for 3/2-in. v-gutter near blow-out and stoichiometric fueling conditions.

Figure 14 contains data for the 3/8-in. v-gutter flame holder at a Reynolds number of 7000, near blow out (left), and at an equivalence ratio of ~ 1.0 , where the first longitudinal mode is excited (right). In the figure are two high-speed images. For the flame near blow out, the sound spectrum is different from that of the 3/2-in. v-gutter. The power in the spectrum is much lower, but two peaks are present—one at ~ 150 Hz and one at ~ 205 Hz. Again according to Huelskamp et al. (2010), the Strouhal number for a v-gutter at the inlet Reynolds number for this experiment is ~ 0.27 , which corresponds to a shedding frequency of ~ 220 Hz. It appears from the data, as in the previous case, that there is sound radiation in the low frequency, with a peak in the range of the Strouhal number of the flame holder

The lower plot in Fig. 14 is for the same flame holder at the same conditions, except that the equivalence ratio is ~ 1.0 . Note that the spectrum above 0 dB now extends down to 400 Hz. Also note several peaks in the pressure data. The energy, however, is much smaller than that of the 3/2-in. flame holder. One of the peaks is near the same frequency as the resonant peak for the 3/2-in. flame holder. As in the case of the 3/2-in. flame holder, other peaks are present in the pressure spectrum. The data seems to indicate that the flame holder with the higher equivalence ratio also radiated sound over a wider spectrum and that several peaks are present in the pressure being radiated. The origin of these peaks is unclear from the pressure data alone. As in the case of the 3/2-in. flame holder, data from heat release and vorticity are required to determine the origin of these peaks.

To gain a better understanding of the coupling between heat-release fluctuations in the flame luminosity and in the pressure spectrum, time-series data were compared. Figure 15 shows the mean luminosity behind the 3/8-in. flame holder at a Reynolds number of 7000 and an equivalence ratio of 0.70. The flame clearly is not near blowout and not exciting a resonant mode. Time series of the instantaneous flame luminosity were acquired from the high-speed camera in the wake (at Point 1 on the figure) and in the shear layer (at Point 2).

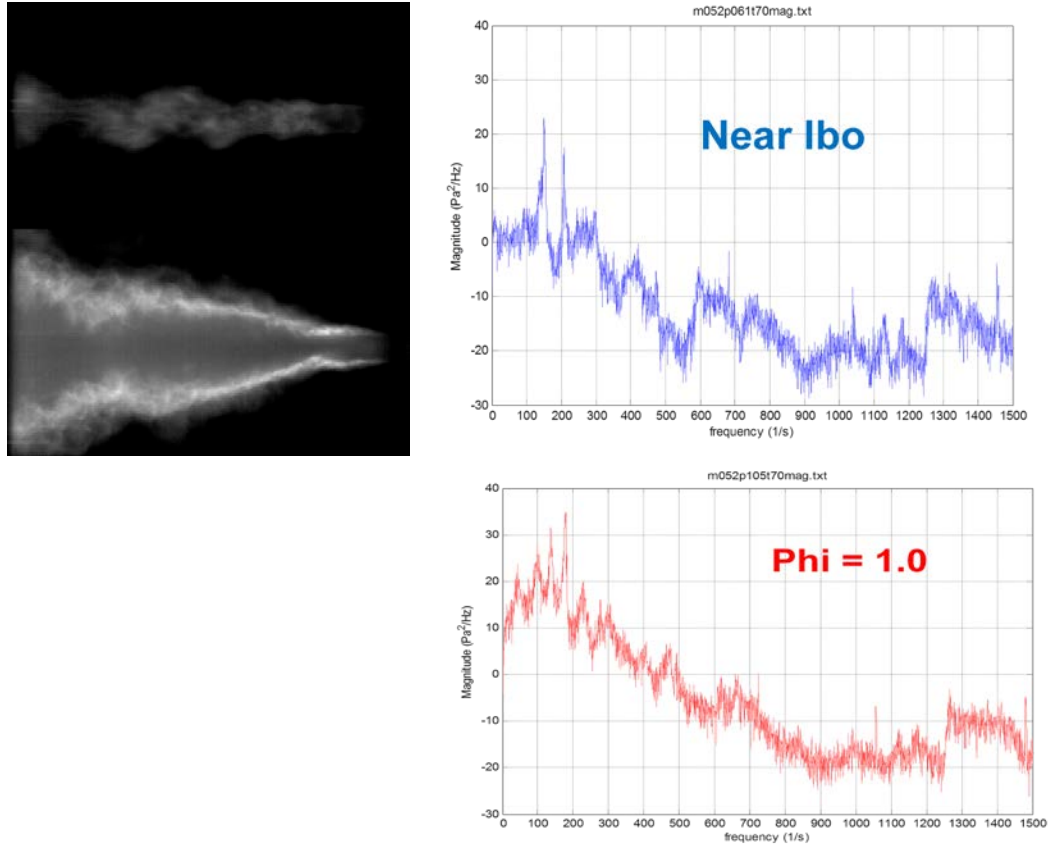


Figure 14. Still image of flame luminosity, magnitude of cross power spectrum of acoustic pressure for 3/8-in. v-gutter near blow out, and stoichiometric fueling conditions.

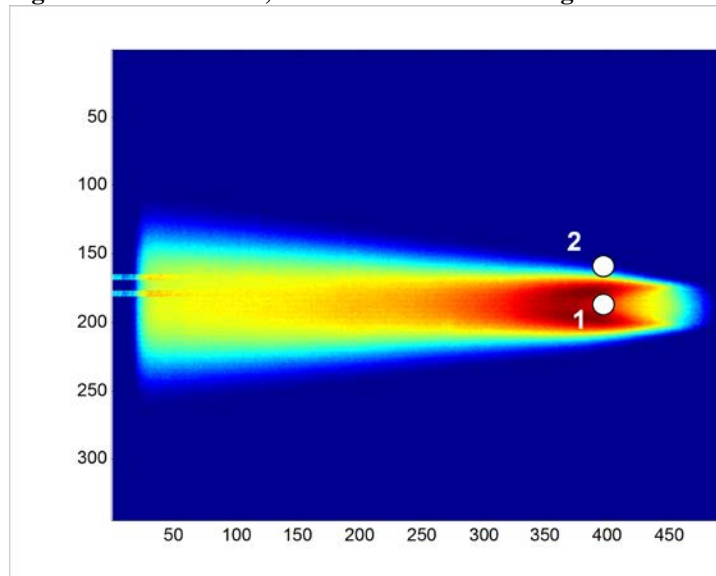


Figure 15. Still image of mean flame luminosity for 3/8-in. v-gutter equivalence ratio of ~0.70.

Regarding the two plots in Fig. 16, the left figure is the power spectrum of the luminosity data at Point 1 on Fig. 15, and the right figure is the autospectrum of the first pressure transducer, located at the pressure antinode of the rig for all modes, (this location is the inlet plate).. First note that the general shape of the plots is very similar. The luminosity is greater than 10^2 below 300 Hz, corresponding to the power in the pressure data below 300 Hz. Also note that the plots have at least five peaks in common in the frequency range between 0 and 300 Hz. This

supports the previous conclusion that the flame is radiating sound, especially in the frequency range between 0 and 300 Hz, and that the sound is being picked up by the SITs. The data presented are necessary but do not offer sufficient proof of the correlation between the flame/vorticity and acoustics.

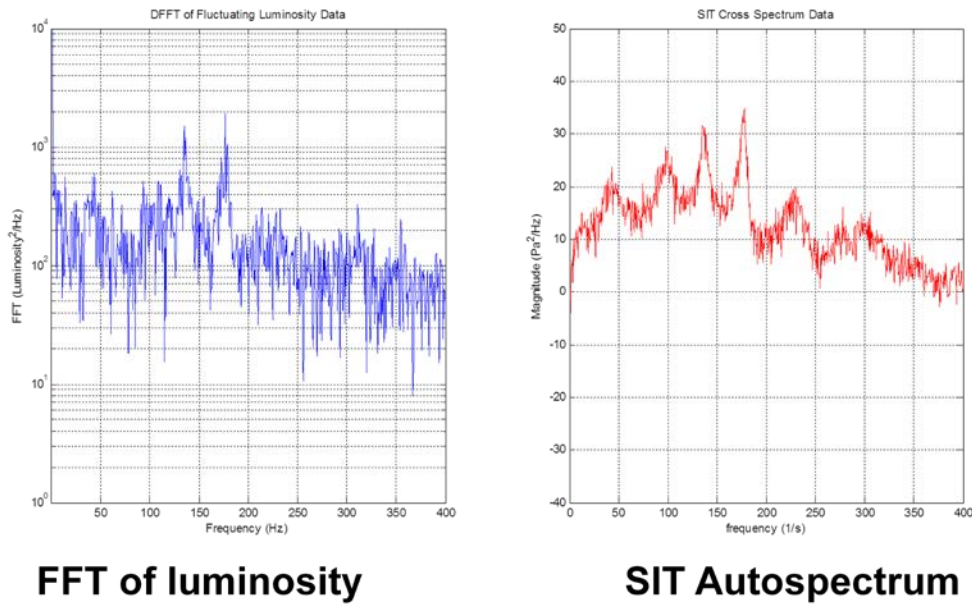


Figure 16. Power spectrum of mean flame luminosity and autospectrum of SIT pressure data for 3/8-in. v-gutter equivalence ratio of ~0.70 located in wake (Point 1).

In Fig. 17 the data on the left-hand side are for the power spectrum of the luminosity at Point 2 on Fig. 15. As in the case of Point 1, the general shape of the plots is very similar. The luminosity is greater than 10² for frequencies below 200 Hz, corresponding to the power in the pressure data below 200 Hz. As in Figure 16, each plot has at least four peaks in common in the frequency range between 0 and 300 Hz. These data corroborate the data and conclusions concerning Fig. 16.

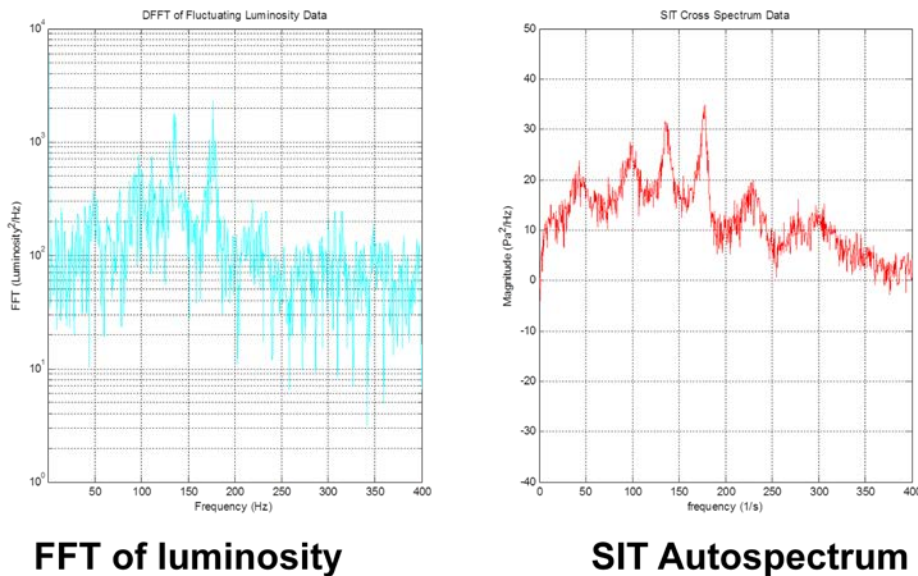


Figure 17. Power spectrum of mean flame luminosity and autospectrum of SIT pressure data for 3/8-in. v-gutter equivalence ratio of ~0.70 located in shear layer (Point 2).

Figure 18, is the cross spectrum of luminosity and pressure obtained simultaneously. The data were taken for the 3/2-in. flame holder at conditions that produced the instability shown in Fig. 12. A point was selected at one diameter downstream of the flame holder, and the luminosity magnitude was saved to a file. Instantaneous pressure data were obtained with a SIT at the pressure antinode. Both the camera and SIT were fired simultaneously in a LabVIEW program. Note the peak in the cross-spectrum data at 122 Hz, which indicates that the pressure and luminosity are highly correlated at that frequency. Also note the large portion of the spectrum above 10 dN, up to 400 Hz.

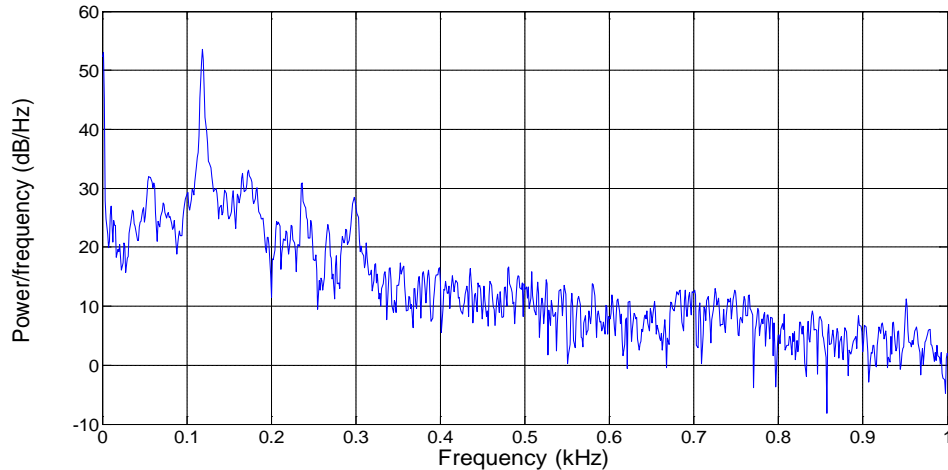


Figure 18. Magnitude of cross power spectrum of instantaneous luminosity and acoustic pressure for self-excited first longitudinal thermoacoustic mode.

VIII. Conclusions

A compressible derivation of the vorticity equation yielded unexpected results. The time-varying vorticity, pressure, and heat release are a single equation. When high-speed images are studied with this equation in mind, it is clear that the vortices captured in the luminosity data can be explained with the vorticity equation. The images lend insight into certain aspects of the vorticity equation, depending on the nature of the heat release depicted in the images. The data support conclusions drawn by previous authors on this subject.

From the pressure data it is clear that the pressure and the flame are linked. Over-the-spectrum increases in acoustic power correspond to increases in luminosity. For flames near blow out, peaks in the pressure data appear to correspond to vortex-shedding frequencies. For the thermoacoustically excited case, the power of the pressure increased 10 dB, and many peaks were noted in the pressure data--one corresponding to the resonant mode of the combustor. The cross spectrum of pressure and luminosity (see Fig. 12) clearly shows a spectral relationship between acoustics and flame luminosity. Both correlate very well at the resonant frequency of the rig.. Combining the experimental data and the vorticity equation, the hypothesis that the flame causes the vorticity to radiate sound across a low-frequency spectrum and that radiation excites a resonance in the chamber is well supported.

At present, a 10-kHz PLIF laser system is being delivered and installed. This laser system will be coupled with a recently delivered 10-kHz PIV system. Simultaneous high-speed PLIF, PIV, and SIT data will be obtained to further explore the coupling of vorticity, heat release, and acoustics as well as the hypotheses that combustion excites vorticity, which radiates sound over a broad spectral range, that discrete vortex frequencies can explain peaks in the pressure data, and that radiated sound couples with rig acoustics to cause thermoacoustic instabilities.

IX. Acknowledgements

The authors would like to thank research technicians Steve Britton, and Dwight Fox for their efforts. We would also like to acknowledge the Turbine Engine Division of the Air Force Research Laboratory for providing the funding necessary to conduct this research.

X. References

- Annaswamy, A.M., et al, 1997, "Impact of Linear Coupling on the Design of Active Controllers for Thermoacoustic Instability," *Combustion Science and Technology* **128**, 131-180.
- Candel, S., 2002, "Dynamics of confined premixed flames submitted to upstream acoustic modulations," *Proceeding of the Combustion Institute* 31 (2007) 1257-1265.
- Culick, F.E.C., 2000, "Combustion Instabilities: Mating Dance of Chemical, Combustion, and Combustor Dynamics." AIAA Paper 2000-3178.
- Culick, F.E.C., 1976, "Nonlinear Behavior of Acoustic Waves in Combustion Chambers," *Acta Astronautica* **3**, 715-756.
- Cummings, A., 1977, "Ducts with Axial Temperature Gradients: An Approximate Solution for Sound Transmission and Generation," *Journal of Sound and Vibration* **51**, 55-67.
- Dowling, A.P., 1995, "The Generation of Thermoacoustic Oscillations," *Journal of Sound and Vibration* **180**(4), 557-581
- Dowling, A.P., and Stow, S.R., 2003, "Acoustic Analysis of Gas Turbine Combustors," *Journal of Propulsion and Power* **19**(5), 751-764.
- Eisenberg, N., and Kao, T., 1969, "Propagation of Sound through a Variable Area Duct with a Steady Compressible Flow," *Journal of the Acoustical Society of America* **49**, 169-175.
- Erickson, R., Soteriou, M., and Prashant, M., 2006, "The Influence of Temperature Ratio on the Dynamics of Bluff Body Stabilized Flames," AIAA Paper 2006-753.
- Ghoniem, A., 1999, "Fundamentals and Modeling in Combustion" *Combustion Science and Technology*, **2**, 280.
- Gogate, G., and Munjal, M., 1992, "Analytical Solution of the Laminar Mean Flow Wave Equation in a Lined or Unlined Two-dimensional Rectangular Duct," *Journal of the Acoustical Society of America* **92**(5), 2915-2923.
- Ingard, U., and Singhal, V., 1973, "Upstream and Downstream Sound Radiation into a Moving Flow," *Journal of the Acoustical Society of America* **45**(4), 1343-1346.
- Ingard, U., and Singhal, V., 1973, "Emissions of Higher-Order Acoustic Modes into a Moving Fluid in a Duct," *Journal of the Acoustical Society of America* **56**(3), 805-808.
- Karthik, B., Mohanraj, R., Ramakrishnan, R., and Sujith, R., 1999, "Exact Solution for Sound Propagation in Ducts with an Axial Mean Temperature Gradient and Particulate Damping," *Journal of the Acoustical Society of America* **106**, 2391-2395.
- Karthik, B., Manoj Kumar, B., and Sujith, R., 2000, "Exact Solution to One-Dimensional Acoustic Fields with Temperature Gradient and Mean Flow," *Journal of the Acoustical Society of America* **108**, 38-43.
- Kumar, B., and Sujith, R., 1998, "Exact Solution for One Dimensional Acoustic Fields in Ducts with Polynomial Mean Temperature Profiles," *ASME Journal of Vibration and Acoustics* **120**, 965-969.
- Malhorta, S., 2004, "On Combustion Instabilities in Solid Rocket Motors," Ph.D. Thesis, California Institute of Technology.
- Mehta, P.G., and Soteriou, M.C., 2003, "Combustion Heat Release Effects on the Dynamics of Bluff Body Stabilized Premixed Reacting Flows," AIAA Paper 2003-0835.
- Morse P., and Ingard, U., 1968, *Theoretical Acoustics*, McGraw Hill, NY
- Nicoud, F., and Poinso, T., 2005, "Thermoacoustic instabilities: Should the Rayleigh criterion be extended to include entropy changes" *Combustion and Flame*, v 142, n 1-2, p 153-159, July 2005
- Pagneux, V., and Froelich, B. 2001, "Influence of Low Mach Number Shear Flow on Acoustic Propagation in Ducts," *Journal of Sound and Vibration* **246**(1), 137-155.
- Pota, H. R., and Kelkar, A. G., 2001, "Modeling and Control of Acoustic Ducts", *Journal of Vibration and Sound* **123**, 2-11
- Richardson, E. G., 1949, *Sound*, 2nd Edition, Edward Arnold and CO, London, pp. 161-164.
- Shanbhogue, S., J., Husain, S., and Lieuwen T., 2009, "Lean Blowoff of Bluff Body Stabilized Flames: Scaling and Dynamics," *Progress in Energy and Combustion Science* **35**, 98-120.
- Subrahmanyam, P., Sujith, R., and Lieuwen, T., 2003, "propagation of Sound in Inhomogeneous Media: Exact, Transient Solutions in Curvilinear Geometries," *Journal of Vibration and Acoustics* **125**, 133-136.
- Sujith, R., Waldherr, G., and Zinn, B., 1995, "An Exact Solution for One-Dimensional Acoustic Fields in Ducts with an Axial Temperature Gradient," *Journal of Sound and Vibration* **184**, 389-402.
- Wood, A. B., 1957, *A Textbook of Sound*, 3rd Edition, Neill and Co. LTD, London, pp. 179-182.